CHORUS

Rectified Rotational Dynamics of Mobile Inclusions in Two-Dimensional Active Nematics

Rectified Rotational Dynamics of Mobile Inclusions in Two-Dimensional Active Nematics

Sattvic Ray,[1] Jie Zhang,[2,3] and Zvonimir Dogic[1]

[1]*Department of Physics, University of California at Santa Barbara, Santa Barbara, California 93106, USA*

[2]*Key Laboratory of Precision and Intelligent Chemistry, University of Science and Technology of China (USTC), Hefei, China.*

[3]*CAS Key Laboratory of Soft Matter Chemistry, Department of Polymer Science and Engineering, University of Science and Technology of China (USTC), Hefei, China.*[*]

(Dated: April 26, 2023)

We investigate the dynamics of mobile inclusions embedded in 2D active nematics. The interplay between the inclusion shape, the boundary-induced nematic order, and the autonomous flows powers the inclusion motion. Disks and achiral gears exhibit unbiased rotational motion, but with distinct dynamics. In comparison, chiral gear-shaped inclusions exhibit long-term rectified rotation, which is correlated with dynamics and polarization of nearby $+1/2$ topological defects. The chirality of defect polarities and the active nematic texture around the inclusion correlate with the inclusion's instantaneous rotation rate. Inclusions provide a promising tool for probing the rheological properties of active nematics and extracting ordered motion from their inherently chaotic motion.

Active matter is composed of energy-consuming constituents whose interactions generate large-scale dynamical patterns [1]. A particular realization of these materials are active nematic liquid crystals, which are composed of motile anisotropic particles with head-tail symmetry. Active nematics exhibit autonomous chaotic flows which are driven by internally generated active stresses that are proportional to the local particle alignment [2–10]. Their dynamics are closely associated with the creation and annihilation of topological defects, which acquire motility from the active stresses [11–19]. Transforming the inherently chaotic dynamics of active nematics into predetermined spatiotemporal patterns that can perform useful functions remains a challenge. One method of controlling active fluids is through boundaries and geometrical confinement. For example, static boundaries can stabilize isolated vortices and arrays of vortices of active fluids [20, 21]. Furthermore, rigid boundaries can also generate unidirectional coherent flows on macroscopic scales and control the periodic nucleation and motion of topological defects in active nematics [22–27]. In a complementary direction, active fluids can interact with rigid but motile boundaries that are advected by autonomous flows. A foundational example is the rectified rotation of a chiral gear-shaped particle powered by motile bacteria [28, 29]. The individual bacteria interacted with the boundaries, generating asymmetric forces which powered persistent rotational motion. In comparison, little is known about how rigid movable boundaries interact with nematically-ordered active fluids. Numerical work explored the dynamics of Janus colloids and arrays of disks free to rotate but not translate in active nematics [30, 31]. Experiments showed that externally rotated disks *above* the active nematic layer can control topological defect dynamics [32]. However, the full range of interaction mechanisms between active nematics and rigid inclusions with translational and rotational degrees of freedom remains unexplored.

To address this knowledge gap, we studied the dynamics of movable inclusions embedded in a 2D microtubule-based active nematic. We observed complex interplay and feedback between the motion of the inclusion and the nematic texture of the enveloping liquid crystal. The inclusion boundaries control the formation and spatiotemporal patterning of topological defects. In turn, the defects and associated nematic texture exerted stress on the inclusion, producing persistent rotations. When combined with work which explored how active fluids couple to liquid interfaces and membranes [33–38], our experiments demonstrate the need to develop a unified theoretical framework for quantitative understanding of interactions between active fluids and movable, deformable and reconfigurable boundaries.

We developed a method to robustly embed a single particle into a 2D active nematic and observe its dynamics over the sample lifetime [Fig. 1a]. We first created an oil-water interface inside an open tube with 3.3 mm diameter. The dense oil and lighter aqueous layers were ∼0.4 mm and ∼1.5 mm high, respectively. We fabricated rigid, quasi-2D particles from SU8 photoresist with size of a few 100 μm [39]. The open tube setup allowed us to deposit a single particle in each sample [Fig. 1b], eliminating unwanted particle-particle interactions. We then assembled a microtubule (MT)-kinesin active nematic around the particle adsorbed at the oil-water interface (see Supplementary Material for further details, which includes Refs [40–43]). The MTs were excluded from the inclusion and aligned parallel to the boundaries. MT bundles sometimes crept under the inclusion, leading to only partial embedding in the nematic layer. To control for embedding quality, we only studied well-embedded inclusions [Fig. S1]. The imaging setup captured the entire interface, allowing us to track the inclusion as well as the active nematic texture over the sample lifetime.

We first studied the translational motion of disk-shaped inclusions of radius r=187.5 μm [Fig. 1b]. For
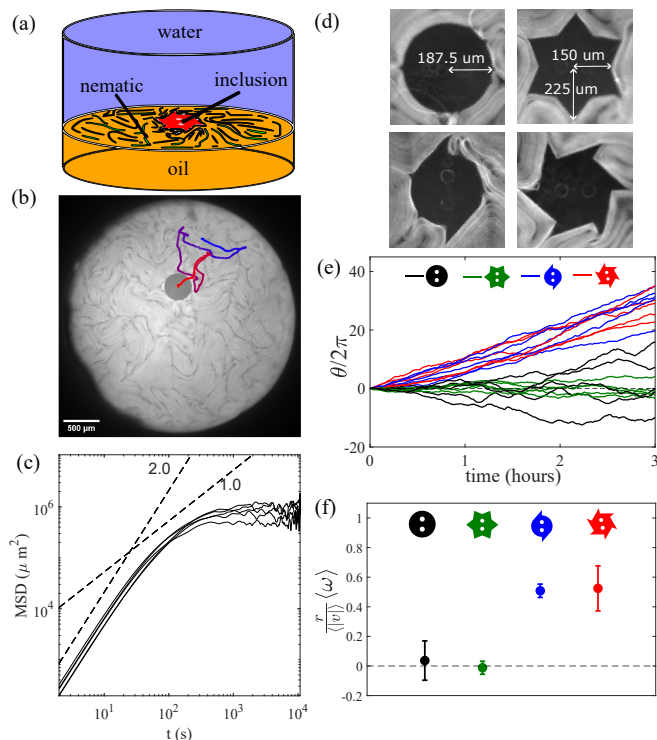
FIG. 1. Inclusions in 2D active nematics. (a) An SU-8 inclusion is placed on an oil-water interface, and a MT-kinesin active nematic is formed around it. (b) An isolated inclusion embedded in the active nematic. The colored line indicates the inclusion trajectory over 17 minutes (t=0 min is blue, and t=17 min is red). (c) MSDs of 5 trajectories of disk-shaped inclusions, each from an independent sample. (d) The four inclusion shapes used in this study. (e) Angular trajectories of different inclusion shapes. Each line corresponds to a single inclusion. For asymmetric gears, $\theta(t)$ trajectories were multiplied by -1 for gears with the opposite chirality than the legend cartoon. (f) Mean rescaled rotation rates of the 4 shapes. The average rotation rate $\langle\omega\rangle$ (rad/s) is rescaled by $\langle| v |\rangle/r$ (1/s) where nematic mean speed is $\langle|v|\rangle$ and inclusion radius is r. Error bars indicate standard deviation over 5 independent samples.

times up to ~45 s, corresponding to displacements of ~280 μm, the motion was along straight lines and the measured mean-squared displacement (MSD) was ballistic [Fig. 1c]. At longer times, the motion transitioned into a diffusive-like regime, which was quickly followed by a plateau of ~1 mm induced by the finite system confinement (3.3 mm diameter). Observation of a truly diffusive regime is complicated by the confinement effects. The correlation length of the active nematic velocity field was ~240 μm, close to the cutoff for ballistic displacements (see Supplementary Material for details on the velocity field measurement, which contains Ref [44]).

Next, we quantified the rotational dynamics of achiral disks, 6-teeth achiral and chiral gears and 2-teeth chiral gears [Fig. 1d]. All gear-like inclusions had an inner radius r_i=150 μm and outer radius r_o=225 μm (corre-

sponding to the base and tip of the teeth, respectively). Thus, their mean radius matched the disks. The MSDs of these shapes were similar to those of the disk [Fig. S3]. However, their rotational dynamics were distinct. Disk and achiral gears switched repeatedly between rotations with opposite directions. In contrast, both the chiral 2-teeth and 6-teeth gears rotated persistently in one direction. Intriguingly, the chiral 2-teeth and 6-teeth gears rotated at essentially the same rate. The rotation direction was set by the handedness of the inclusion chirality [Fig. 1e, Supplementary Videos 1-4].

The active nematic system had significant sample-to-sample variability in the mean speed [Fig. S4a]. To compare data across different samples, we rescaled the inclusion's mean rotation rate $\langle\omega\rangle$ by $\langle|v|\rangle/r$, where $\langle|v|\rangle$ is the mean speed of the background nematic averaged over space and time, and r is the inclusion radius (or an average of outer and inner radii, in the case of gears) [Fig. 1f]. The rescaled rotation rate was ~0 for disks and achiral gears, and ~0.5 for both the chiral 2-teeth and 6-teeth gears. Thus, on average, the tangential velocity of the inclusion boundary was about half the speed of the nematic for both chiral 2-teeth and 6-teeth gears. For all inclusions, the instantaneous rotation rate was correlated with the instantaneous mean speed of the active nematic [Fig. S4b].

Both disks and achiral gears failed to show persistent rotation over long timescales. Nevertheless, they exhibited distinct rotational dynamics. In contrast to gears, disks rotated longer in one direction before switching. This distinction is captured by the temporal autocorrelation of the mean-subtracted angular velocity [Fig. 2a]. For each shape, we defined an average fluctuation timescale as the lag time at which the autocorrelation dropped to 0.5. The fluctuation timescale for the disks was about three times longer than the gears, which all had timescales close to those of the background active nematic [Fig. 2b]. Thus, disks stabilized long-lived vortical flows.

To gain insight into the mechanism driving these rotational dynamics, we studied the organization of the active nematic around the inclusions [Supplementary Videos 5-8]. In bulk 2D extensile active nematics, pairs of oppositely charged defects are constantly created and annihilated [4, 12, 13] (see Supplementary Material for details about quantifying the nematic field and locating defects, which contains Refs [45–48]). Due to their asymmetry, the $+1/2$ defects move in the direction of their polarity. Boundaries influence defect dynamics. In the vicinity of a chiral tooth, $+1/2$ defects exhibited cyclic dynamics [Fig. 3a]. At the beginning of each cycle, a $+1/2$ defect aligned with the long edge of a tooth while pointing against the short edge of the adjacent tooth. Subsequently, as the motile defect approached the corner, it turned away from the inclusion moving along the shorter edge. This motion generated a bend deformation, which
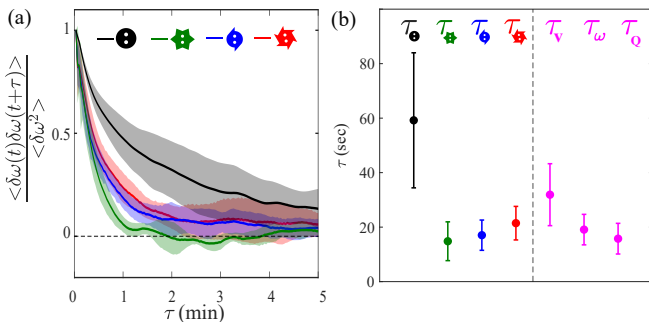
FIG. 2. Inclusion shape controls the fluctuations in angular velocity. (a) Auto-correlation of the mean-substracted angular velocity. Shaded regions indicate the standard deviation from different trajectories (n=5). (b) Average fluctuation timescales τ_{shape} for the different inclusion shapes, and characteristic timescales of bulk active nematic. τ_{shape} is the lag time at which the autocorrelation reaches 0.5. Similarly, τ_v, τ_ω, and τ_Q are the lag times at which the velocity, vorticity, and Q-tensor autocorrelation of the background nematic field, respectively, reach 0.5. Error bars indicate standard deviation (n=5).

nucleated a new defect pair. The +1/2 defect from the newly nucleated pair aligned with the long edge of the tooth, initiating the next cycle.

To elucidate the relationship between defect organization and inclusion shape, we measured the average polarization of +1/2 defects within a 150 μm wide (twice the tooth height) annular region around the inclusion [Fig. 3b]. We computed the tangential component of the polarity of each +1/2 defect detected in this region, $p_t \equiv (\mathbf{r} \times \mathbf{p}) \cdot \hat{\mathbf{z}}/r$, with $\mathbf{r}$ the displacement from the inclusion center and $\mathbf{p}$ the defect polarity (unitary length) [Fig. 3c]. The polarization distributions were strongly skewed towards $p_t = 1$ for the chiral gears but were symmetric for the achiral gears and disks [Fig. 3d]. Since +1/2 defects self-propel in the direction of their polarization, these distributions suggest that defects with $p_t > 0$ ($p_t < 0$) impart positive (negative) torque to the inclusion, rotating it counterclockwise (clockwise).

In addition to angular polarization, the inclusions also controlled the radial density distribution of topological defects [Fig. 3e]. The -1/2 defects accumulated at the boundary of disks, with a corresponding buildup of +1/2 defects away from the boundary. In contrast, the chiral 6-teeth gears induced a strong buildup of +1/2 defects, but not -1/2 defects, in the region between the teeth. This is consistent with the previously discussed boundary-induced alignment and nucleation of +1/2 defects. The defect density profile of chiral 2-teeth gears shared characteristics with both the disk and chiral 6-teeth gears. The chiral 2-teeth gears featured both a buildup of -1/2 defects near the boundary away from the teeth and a buildup of +1/2 defects near the teeth. Unlike the chiral 6-teeth gear, the achiral 6-teeth gear
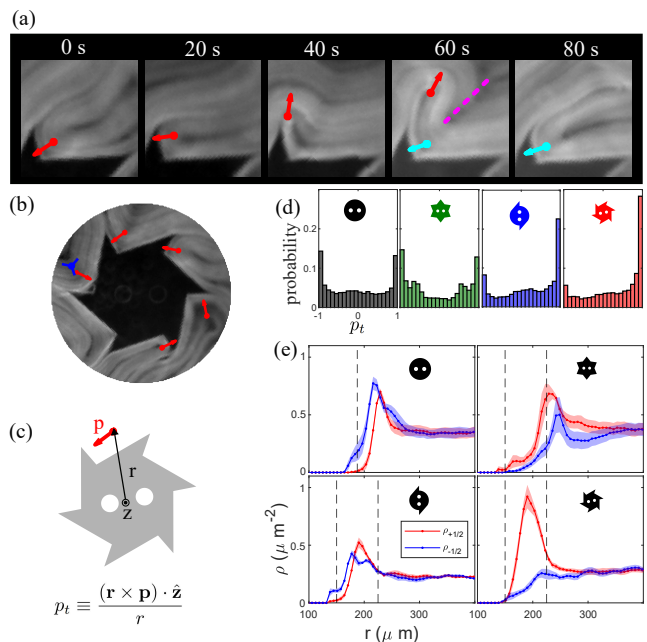

FIG. 3. Behavior of topological defects near inclusions. (a) Active nematic defects cycle observed near a corner of the chiral 6-teeth inclusion. The first +1/2 defect is shown in red, the second in cyan. The dashed magenta line indicates a bend deformation causing the nucleation of the second +1/2 defect. (b) Defects detected in the inclusion vicinity. The annular width of the region is twice the width of the inclusion teeth. +1/2 defects are red, -1/2 defect are blue. (c) Polarity of a +1/2 defect. (d) Distribution of defect polarities near inclusions for the four different shapes. Each histogram corresponds to defects detected during the first 33 minutes of a single sample. (e) Radial distribution of defect densities as a function of distance from the inclusion center. For the disk, the dashed line indicates the disk radius. For the toothed shapes, the first and second dashed lines indicate the inner and outer radii, respectively. The curve thickness indicates the standard error (n=5).

induced a buildup of both +1/2 and -1/2 defects just beyond the tips of the teeth. Thus, simply changing the aspect ratio and chirality of the 6 teeth significantly alters the defect density profile.

Next, we aimed to correlate inclusion-induced defect structure to inclusion rotational dynamics. In each frame, we compared the net tangential polarization of all +1/2 defects within the annulus, $p_{t,net}(t)$, to the instantaneous inclusion's rotation rate $\omega(t)$ [Fig. 4b]. For all shapes, $\omega(t)$ was weakly correlated with $p_{t,net}(t)$, with a Pearson cross-correlation of $\rho_{\omega,p} \sim$0.2-0.6 [Fig. 4c]. Defect polarizations alone may not capture the full coupling of the nematic texture to the inclusion rotation rate, as the deformations of the defect-free regions of the nematic field may impart significant stress to the inclusion. To overcome this issue, we also calculated gradients of the nematic order parameter Q:
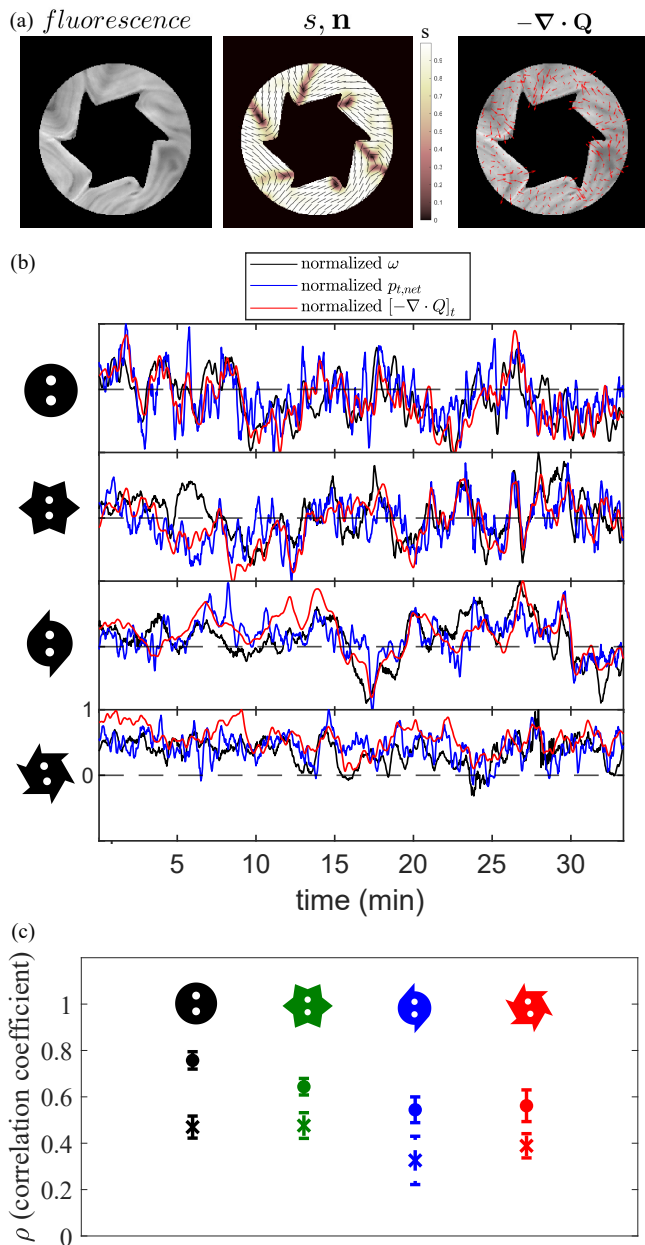
FIG. 4. Correlating defect structure to inclusion motion. (a) Computation of $-\boldsymbol{\nabla}\cdot\mathbf{Q}$ from a fluorescence image of MTs. From the image (left), the nematic order parameter $\mathbf{Q} = s(\mathbf{nn} - \frac{1}{2}\mathbf{1})$ is computed. The fields s and $\mathbf{n}$ are displayed (center), as well as $-\boldsymbol{\nabla}\cdot\mathbf{Q}$ (right). (b) Time-series of the normalized angular rotation rate, net $+1/2$ defect polarization, and the average tangential component of $-\boldsymbol{\nabla}\cdot\mathbf{Q}$ inside an annulus around each of the 4 shapes. Each time-series is smoothed with moving mean window of width 10 s. (c) Pearson correlation coefficients between the normalized rotation rate and normalized net polarization or Q-tensor tangential gradient, after these timeseries are smoothed as above. The crossed points indicate the former ($\rho_{\omega,p}$), while the solid points indicate the latter ($\rho_{\omega,Q}$). Error bars represent standard error of the mean over 5 independent experiments for each shape.

$$\langle[\boldsymbol{\nabla}\cdot\mathbf{Q}]_t\rangle_A \equiv -\iint_A \frac{(\mathbf{r}\times\boldsymbol{\nabla}\cdot\mathbf{Q})\cdot\hat{\mathbf{z}}}{r} \qquad (1)$$

where A denotes an annular region around the inclusion. This quantity is motivated by continuum theories of active nematic hydrodynamics, where active stress is $\sigma_a = \alpha\mathbf{Q}$. For extensile MT-kinesin active nematics, $\alpha < 0$. The active force field imparted to the fluid is then $\mathbf{f}_a \propto -\boldsymbol{\nabla}\cdot\mathbf{Q}$. Thus, $\langle[\boldsymbol{\nabla}\cdot\mathbf{Q}]_t\rangle_A$ is the average tangential component of the active forces in a region around the inclusion. The nematic order parameter $\mathbf{Q} = s(\mathbf{nn} - \frac{1}{2}\mathbf{1})$ and its divergence are computed from the fluorescence images [Fig. 4a] (see Supplementary Material for details). We found that the $\langle[\boldsymbol{\nabla}\cdot\mathbf{Q}(t)]_t\rangle_A$ was a more accurate predictor of the rotation rate $\omega(t)$ than $p_{t,net}(t)$, with a cross-correlation of $\rho_{\omega,Q} \sim 0.4$-0.8 for all shapes [Fig. 4c]. Active forces $\propto -\boldsymbol{\nabla}\cdot\mathbf{Q}$ generated away from the inclusion can only influence inclusion motion through the mediating solvent. A complete modeling scheme would require measuring or numerically solving for the fluid flow at the inclusion boundary, and then estimating the active, viscous, and passive elastic stresses. Intriguingly, a quantity involving only the nematic Q-tensor captures the main features of the inclusion's rotational dynamics.

Our experiments demonstrated the rich behavior of inclusions embedded in 2D active nematics. Chiral gear-shaped inclusions rotated persistently in one direction, while achiral disks and gears did not. Intriguingly, the chiral 2-teeth and 6-teeth gears rotated at the same average rate, with a tangential velocity about half the speed of the bulk active nematic. This contrasts with a study where the circulation speed of a 3D isotropic active fluid confined to an annulus decreased with the number of notches on the boundary [22]. Another study observed the persistent unidirectional circulation of an active nematic confined inside a 200 μm well with a single chiral notch on the boundary [23]. In that case, the notch also served as a site for defect nucleation, although the notch shape and nucleation process were different. For smooth circular confinement without a notch, the same study found that the active nematic organized into a vortical flow, with the sign of vorticity sometimes reversing. This may be related to the behavior of the disk-shaped inclusion in our experiments, whose angular velocity fluctuations were correlated over longer timescales than those of any of the gears. Taken together, these results suggest that smooth boundaries can induce spontaneous and persistent vorticity in active nematics, but this has yet to be systematically explored.

Our system has both similarities and differences with studies of gears powered by motile bacteria [28, 29]. In both cases, chiral gears rotated unidirectionally, while achiral gears did not. In our study, the chiral gears at the oil-water interface of an active nematic always rotated towards the slanted edges of the teeth, just as chiral gears

at the air-water interface of a bacterial suspension. As polar swimmers, individual bacteria were more likely to get trapped along the long edge while pointing towards the short edge. The bacteria exerted force by direct contact on the short edges, leading to a net torque. While built from apolar constituents, active nematics exhibit $+1/2$ topological defects which are polar quasi-particles. Moreover, the dynamics of $+1/2$ defects near the chiral teeth [Fig. 3a] suggest that they play an analogous role to the swimming bacteria, pushing more against the short edge than the long edge and therefore transferring net torque to the gear. A key difference, however, is that defects are continuously created and annihilated within an active nematic, and this regeneration is boundary controlled. The presence of the chiral teeth induces the local cyclic nucleation of $+1/2$ defects [Fig. 3a], rather than capturing defects from the bulk. Unlike bacteria, forces exerted by the defects on the inclusion cannot come from direct contact. The active, elastic, and viscous stresses felt at the inclusion boundary are caused by the hydrodynamic flows and associated nematic texture. Our experiments demonstrate a need to understand the effective interaction between defects and inclusion boundaries in active nematics.

The possibility of using inclusions to extract work from chaotic active nematics is intriguing. Approximating the chiral gears as disks, the power dissipated by their rotation may be estimated as $P_{rot} \sim 32/3 r \nu_0 \Omega^2 \sim 3 \times 10^{-17}$ W, with $\nu_0 \sim 10^{-3}$ Pa-s the viscosity of water, $r \sim 200$ μm the disk radius, and $\Omega \sim 0.02$ rad/s the average rotation rate [28, 29]. Following estimates of the power of 3D active fluids [49], the power dissipated by the flows of a 2D active nematic patch with the same area as the inclusion may be estimated as $P_{flow} \sim \nu_n \left(v^2/L^2 \right) A_0 \sim 5 \times 10^{-17}$ W, with $\nu_n \sim 1$ Pa-s-μm the 2D viscosity of the nematic layer [32, 50], $v \sim 5$ μm/s the typical speed of the active flows, $L \sim 250$ μm the length scale over which flows are correlated, and $A_0 \sim 400$ μm^2 the inclusion area . Thus, the power harnessed as gear rotation is comparable to the viscous dissipation of the active nematic. However, the *chemical* power dissipated as heat by ATP hydrolysis orders of magnitude higher than the flow power for MT-kinesin active fluids, which means that the total efficiency of the rotating gear is extremely low [**?**]. Perhaps a more useful quantification of efficiency is the rescaled rotation rate $r \langle \omega \rangle / \langle |v| \rangle$, which was ~ 0.5 for both the chiral 2-teeth and 6-teeth gears. This means that the boundary of the gears move, on average, about half as fast as the bulk active nematic.

From an entirely different perspective, these experiments extend previous work on mixtures of equilibrium liquid crystals and conventional colloids, which demonstrated control of the spatial structure and the topology of defects [51–55], as well as defect-assisted motion of externally driven colloids [56]. Creating active liquid crystal/colloid composites offers a tantalizing possibility of using inclusions in *active* nematics to control both the spatial and temporal dynamics of motile topological defects which in turn affect the colloidal motion [57].

In conclusion, we studied the dynamics of inclusions embedded in 2D active nematics with parallel anchoring. Chiral gear-shaped inclusions rotated persistently in one direction, while disk and achiral gear had unbiased rotation. Inclusion shape influenced the polarization and distribution of nearby topological defects. These results show that inclusion motion in active nematics arises from a delicate interplay between the inclusion shape, organization of the surrounding nematic, and the boundary-induced self-organized active stresses.

All data reported in the main text as well as code for reproducing the analysis will be made available at [58].

* zhjie717@ustc.edu.cn
[1] M. Marchetti, J. Joanny, S. Ramaswamy, T. Liverpool, J. Prost, M. Rao, and R. A. Simha, Review of Modern Physics **85**, 1143 (2013).
[2] R. Aditi Simha and S. Ramaswamy, Phys. Rev. Lett. **89**, 058101 (2002).
[3] V. Narayan, S. Ramaswamy, and N. Menon, Science **317**, 105 (2007).
[4] T. Sanchez, D. T. N. Chen, S. J. DeCamp, M. Heymann, and Z. Dogic, Nature **491**, 431 (2012).
[5] S. Zhou, A. Sokolov, O. D. Lavrentovich, and I. S. Aranson, Proceedings of the National Academy of Sciences **111**, 1265 (2014).
[6] P. Guillamat, J. Ignés-Mullol, and F. Sagués, Proceedings of the National Academy of Sciences **113**, 5498 (2016).
[7] G. Duclos, C. Blanch-Mercader, V. Yashunsky, G. Salbreux, J.-F. Joanny, J. Prost, and P. Silberzan, Nature physics **14**, 728 (2018).
[8] H. Li, X.-q. Shi, M. Huang, X. Chen, M. Xiao, C. Liu, H. Chaté, and H. Zhang, Proceedings of the National Academy of Sciences **116**, 777 (2019).
[9] N. Kumar, R. Zhang, J. J. De Pablo, and M. L. Gardel, Science advances **4**, eaat7779 (2018).
[10] A. J. Tan, E. Roberts, S. A. Smith, U. A. Olvera, J. Arteaga, S. Fortini, K. A. Mitchell, and L. S. Hirst, Nature Physics **15**, 1033 (2019).
[11] X. qing Shi and Y. qiang Ma, Nature Communications **4**, 10.1038/ncomms4013 (2013).
[12] L. Giomi, M. J. Bowick, X. Ma, and M. C. Marchetti, Physical Review Letters **110**, 10.1103/physrevlett.110.228101 (2013).
[13] S. P. Thampi, R. Golestanian, and J. M. Yeomans, EPL (Europhysics Letters) **105**, 18001 (2014).
[14] L. Giomi, Physical Review X **5**, 031003 (2015).
[15] T. Gao, R. Blackwell, M. A. Glaser, M. D. Betterton,

and M. J. Shelley, Physical review letters **114**, 048101 (2015).

[16] E. Putzig, G. S. Redner, A. Baskaran, and A. Baskaran, Soft Matter **12**, 3854 (2016).

[17] S. Shankar, S. Ramaswamy, M. C. Marchetti, and M. J. Bowick, Physical Review Letters **121**, 10.1103/physrevlett.121.108002 (2018).

[18] G. A. Vliegenthart, A. Ravichandran, M. Ripoll, T. Auth, and G. Gompper, Science advances **6**, eaaw9975 (2020).

[19] C. Joshi, S. Ray, L. M. Lemma, M. Varghese, G. Sharp, Z. Dogic, A. Baskaran, and M. F. Hagan, Phys. Rev. Lett. **129**, 258001 (2022).

[20] H. Wioland, F. G. Woodhouse, J. Dunkel, J. O. Kessler, and R. E. Goldstein, Phys. Rev. Lett. **110**, 268102 (2013).

[21] D. Nishiguchi, I. S. Aranson, A. Snezhko, and A. Sokolov, Nat. Commun. **9**, 4486 (2018).

[22] K.-T. Wu, J. B. Hishamunda, D. T. N. Chen, S. J. DeCamp, Y.-W. Chang, A. Fernández-Nieves, S. Fraden, and Z. Dogic, Science **355**, eaal1979 (2017).

[23] A. Opathalage, M. M. Norton, M. P. N. Juniper, B. Langeslay, S. A. Aghvami, S. Fraden, and Z. Dogic, Proceedings of the Natural Academy of Sciences **116**, 4788 (2019).

[24] J. Hardoüin, R. Hughes, A. Doostmohammadi, J. Laurent, T. Lopez-Leon, J. M. Yeomans, J. Ignés-Mullol, and F. Sagués, Communications Physics **2** (2019).

[25] J. Hardoüin, J. Laurent, T. Lopez-Leon, J. Ignés-Mullol, and F. Sagués, Soft Matter **16**, 9230 (2020).

[26] N. Figueroa-Morales, M. M. Genkin, A. Sokolov, and I. S. Aranson, Communications Physics **5**, 1 (2022).

[27] J. Hardoüin, C. Doré, J. Laurent, T. Lopez-Leon, J. Ignés-Mullol, and F. Sagués, Nature communications **13**, 1 (2022).

[28] R. Di Leonardo, L. Angelani, D. Dell'Arciprete, G. . Ruocco, V. Iebba, S. Schippa, M. Conte, F. Mecarini, F. De Angelis, and E. Di Fabrizio, Proceedings of the Natural Academy of Sciences **107**, 9541 (2010).

[29] A. Sokolov, M. M. Apodaca, B. A. Grzybowski, and I. S. Aranson, Proceedings of the Natural Academy of Sciences **107**, 969 (2010).

[30] B. Loewe and T. N. Shendruk, New Journal of Physics **24**, 012001 (2022).

[31] S. P. Thampi, A. Doostmohammadi, T. N. Shendruk, R. Golestanian, and J. M. Yeomans, Science Advances **2**, 10.1126/sciadv.1501854 (2016).

[32] D. P. Rivas, T. N. Shendruk, R. R. Henry, D. H. Reich, and R. L. Leheny, Soft Matter **16**, 9331 (2020).

[33] F. C. Keber, E. Loiseau, T. Sanchez, S. J. DeCamp, L. Giomi, M. J. Bowick, M. C. Marchetti, Z. Dogic, and A. R. Bausch, Science **345**, 1135 (2014).

[34] H. R. Vutukuri, M. Hoore, C. Abaurrea-Velasco, L. van Buren, A. Dutto, T. Auth, D. A. Fedosov, G. Gompper, and J. Vermant, Nature **586**, 52 (2020).

[35] S. C. Takatori and A. Sahu, Physical Review Letters **124**, 158102 (2020).

[36] G. Kokot, H. A. Faizi, G. E. Pradillo, A. Snezhko, and P. M. Vlahovska, Communications Physics **5**, 1 (2022).

[37] R. Adkins, I. Kolvin, Z. You, S. Witthaus, M. C. Marchetti, and Z. Dogic, Science **377**, 768 (2022).

[38] Y. Young, M. Shelley, and D. Stein, Mathematical biosciences and engineering **18** (2021).

[39] S. Q. Choi, S. G. Jang, A. J. Pascall, M. D. Dimitriou, T. Kang, C. J. Hawker, and T. M. Squires, Advanced Materials **23**, 2348 (2011).

[40] A. M. Tayar, L. M. Lemma, and Z. Dogic, in *Microtubules* (Springer, 2022) pp. 151–183.

[41] S. J. DeCamp, G. S. Redner, A. Baskaran, M. F. Hagan, and Z. Dogic, Nature materials **14**, 1110 (2015).

[42] M. Castoldi and A. V. Popov, Protein expression and purification **32**, 83 (2003).

[43] R. Subramanian and J. Gelles, The Journal of general physiology **130**, 445 (2007).

[44] W. Thielicke and R. Sonntag, Journal of Open Research Software **9**, 10.5334/jors.334 (2021).

[45] R. Rezakhaniha, A. Agianniotis, J. T. C. Schrauwen, A. Griffa, D. Sage, C. v. Bouten, F. Van De Vosse, M. Unser, and N. Stergiopulos, Biomechanics and modeling in mechanobiology **11**, 461 (2012).

[46] G. Duclos, R. Adkins, D. Banerjee, M. S. Peterson, M. Varghese, I. Kolvin, A. Baskaran, R. A. Pelcovits, T. R. Powers, A. Baskaran, *et al.*, Science **367**, 1120 (2020).

[47] Z. Zhou, C. Joshi, R. Liu, M. M. Norton, L. Lemma, Z. Dogic, M. F. Hagan, S. Fraden, and P. Hong, Soft matter **17**, 738 (2021).

[48] M. M. Norton, https://github.com/wearefor/qcon_nematicdefectfinder (2021).

[49] P. J. Foster, J. Bae, B. Lemma, J. Zheng, W. Ireland, P. Chandrakar, R. Boros, Z. Dogic, D. J. Needleman, and J. J. Vlassak, Proceedings of the National Academy of Sciences **120**, 10.1073/pnas.2207662120 (2023).

[50] B. Martínez-Prat, R. Alert, F. Meng, J. Ignés-Mullol, J.-F. Joanny, J. Casademunt, R. Golestanian, and F. Sagués, Physical Review X **11**, 10.1103/physrevx.11.031065 (2021).

[51] P. Poulin, H. Stark, T. C. Lubensky, and D. A. Weitz, Science **275**, 1770 (1997).

[52] Y. Gu and N. L. Abbott, Phys. Rev. Lett. **85**, 4719 (2000).

[53] I. Musevic, M. Skarabot, U. Tkalec, M. Ravnik, and S. Zumer, Science **313**, 954 (2006).

[54] C. P. Lapointe, T. G. Mason, and I. I. Smalyukh, Science **326**, 1083 (2009).

[55] A. Martinez, T. Lee, T. Asavei, H. Rubinsztein-Dunlop, and I. I. Smalyukh, Soft Matter **8**, 2432 (2012).

[56] T. Yao, Ž. Kos, Q. X. Zhang, Y. Luo, E. B. Steager, M. Ravnik, and K. J. Stebe, Science Advances **8**, 10.1126/sciadv.abn8176 (2022).

[57] M. Rajabi, H. Baza, T. Turiv, and O. D. Lavrentovich, Nat. Phys. **17**, 260 (2021).

[58] S. Ray, J. Zhang, and Z. Dogic, Dryad (2023).